American Society of
Mechanical Engineers

ASME Accepted Manuscript Repository

Institutional Repository Cover Sheet

Zhao, Liguo
First Last

ASME Paper Title: Mechanical behaviour of silicon carbide under static and dynamic compressior

Authors: Zhang, D.
Zhao, Liguo
Roy, Anish

ASME Journal Title: Transactions of the ASME

Volume/Issue 141(1): 011007

Date of Publication (VOR* Online) May 16, 2018

ASME Digital Collection URL: http://materialstechnology.asmedigitalcollection.asme.org/article.aspx?articleid=2688

DOI: 10.1115/1.4040591

*VOR (version of record)

Mechanical Behaviour of Silicon Carbide under Static and Dynamic Compression

D Zhang, LG Zhao* and A Roy

Wolfson School of Mechanical, Electrical and Manufacturing Engineering, Loughborough University, Loughborough, LE11 3TU, UK

*Corresponding author; Email: L.Zhao@Lboro.ac.uk; Tel.: 0044-1509-227799

Abstract

This paper compared the mechanical behaviour of 6H SiC under quasi-static and dynamic compression. Rectangle specimens with a dimension of 3×3×6 mm^3 were used for quasi-static compression tests under three different loading rates (i.e., 10^{-5}/s, 10^{-4}/s and 10^{-3}/s). Stress-strain response showed purely brittle behavior of the material which was further confirmed by SEM/TEM examinations of fractured fragments. For dynamic compression, split Hopkinson pressure bar (SHPB) tests were carried out for cubic specimens with a dimension of 6×6×4 mm^3. Stress-strain curves confirmed the occurrence of plastic deformation under dynamic compression, and dislocations were identified from TEM studies of fractured pieces. Furthermore, JH2 model was used to simulate SHPB tests, with parameters calibrated against the experimental results. The model was subsequently used to predict strength and plasticity-related damage under various dynamic loading conditions. This study concluded that, under high loading rate, SiC can deform plastically as evidenced by the development of non-linear stress-strain response and also the evolution of dislocations. These findings can be explored to control the brittle behaviour of SiC and benefit end users in relevant industries.

Keywords: Silicon carbide; Mechanical behaviour; Static compression; SHPB tests; Plastic deformation; Loading rate.

1. Introduction

Silicon carbide (SiC) is a ceramic material with high strength, superior hardness and strong wear resistance even at elevated temperatures. It also possesses high thermal shock resistance, low thermal expansion and high thermal conductivity. Consequently, it is widely used in microelectromechanical systems (MEMS) [1-3], turbine engine components [4], automobile brakes [5], bulletproof armour [6, 7], cutting tools and abrasives [8] which require high durability and strength. Extensive efforts have been made to explore the mechanical properties of SiC and further promote its applications. For instance, Lankford [9] performed both quasi-static and dynamic compression tests on SiC and found that the compressive strength increased exponentially after a transition strain rate was reached. It was also noticed that micro-cracks nucleated at intrinsic flaws such as twinning and grain boundary junctions under low strain rate. With the increase of strain rate, the micro-crack density increased and the material failed when those cracks coalesced spontaneously to form macro-cracks. The coalescence of micro-cracks was also supported by other researchers and termed as 'wing crack' phenomenon [10, 11]. Sarva and Nemat-Nasser [11] carried out quasi-static and split Hopkinson pressure bar (SHPB) tests on hot-pressed sintered silicon carbide. The samples failed by axial splitting under both static and dynamic loading conditions, with a compressive strength of 4.2 GPa and 7 GPa, respectively. Garkushin [12] compared the mechanical properties of reaction sintered, hot-pressed and synthesized silicon carbide which showed similar density and wave propagation speed but different dynamic elasticity limit and strength. As reported in Holland and McMeeking [13], the quasi-static strength of SiC was governed by fracture toughness and the size of flaws embedded in the material while the transition strain rate was influenced by both material properties and microstructures.

In addition, Pittari [14] carried out a series of experiments to understand how the mechanical properties varied with the composition and manufacturing processes for SiC. Pressureless-sintered and reaction-bonded SiCs were tested under quasi-static and dynamic loading conditions. It was found that fracture toughness was affected by both manufacturing processes and loading rates. The presence of a residual silicon phase in reaction-bonded SiC caused the difference in fracture toughness, which was associated with tortuous crack path, mismatch of thermal expansion coefficients and compressive residual stresses. It was also found that dynamic fracture toughness was higher than static one due to the less amount of time allowed for the crack to nucleate and grow under dynamic loading condition. Microcracks intended to nucleate in multiple points due to the inertial dependence of crack initiation and propagation was also reported in Lankford [9]. Specifically, radial expansion was delayed due to the inertia-induced confinement in the radial direction, and therefore the propagation of micro-cracks was inhibited by the time-dependent confining mechanism. Holland and McMeeking [13] suggested that the dynamic fracture strength was also related to the material density. Above a threshold value (density), the dynamic strength was shown to be affected by material density and generally exceeded the quasi-static strength. Also, the larger the Young's modulus, the lower the transition strain rate (i.e., a greater rate sensitivity in the dynamic regime). The rate sensitivity increased with increasing Poisson's ratio, but no such effect was shown for the transition strain rate and quasi-static strength.

Although extensive research efforts have been made regarding the mechanical behaviour of SiC, they were mostly focused on the rate sensitivity and cracking behaviour. To the best knowledge of the authors, there are very limited studies into the plastic deformation of SiC in various conditions including high-speed impact and confined compression. For ceramics, high homologous temperatures are normally the key requirement for plastic deformation to occur. At

room temperature, the material has intrinsic resistance to dislocation nucleation and movement, causing brittleness of ceramics and failure by crack propagation. Despite the general assumption that ceramics are brittle, plastic deformation caused by dislocation movement or crystallographic slip occurs at ambient temperature. Numerous studies have been carried out to study plastic deformation in ceramics. For instance, Castaing et al. [15] found that dislocation-associated plastic deformation occurred in Al_2O_3 under quasi-static compression when temperature was greater than 200°C. Lankford [16] tested Al_2O_3 at different temperatures (-196°C to 1526°C) and different strain rates (10^{-5}/s to 10^{3}/s), and found that transgranular cracking, nucleated by twinning process (plastic deformation), was the dominant failure mechanism at low temperature and under quasi-static loading conditions. Louro and Meyers [17] found that ceramic materials failed by dislocation movement in an impact test with lateral confinement, even at ambient temperature. Tests performed by Chen and Ravichandran[18] on AlN (aluminium nitride) also showed plastic deformation in failure, and the failure mode changed from fragmentation by axial splitting to localized faulting under lateral confinement.

In this paper, both quasi-static and SHPB tests were performed on pressureless-sintered polycrystalline 6H-SiC to investigate the regime of plastic deformation of this material. Different strain rate was adopted to study the static and dynamic deformation behaviour under uniaxial compression. Stress-strain behaviour was recorded, and post-test SEM and TEM analyses were conducted to determine the failure mode and the relationship between microstructure and failure strength. In addition, numerical simulations were carried out to study the effect of loading rate on compressive strength, with the incorporation of plastic deformation.

2. Experimental details

2.1 Material and Specimen

The material used for the tests is Hexoloy SA silicon carbide, which was produced by pressure-less sintering of submicron silicon carbide powder at temperature above 2000°C. The sintered sample has fine grains, and the grain size ranges from 4 to 10 microns (Fig. 1). The as-received silicon carbide tiles were of hexagonal shape with a side length of 27 mm and a thickness of 4 mm (Fig. 2a). These were cut into cuboidal samples using a diamond blade fitted on the Accutom 5 machine. Two sets of specimens were cut, with a nominal dimension of 3×3×6 mm^3 and 6×6×4 mm^3 for quasi-static and dynamic (SHPB) compression tests, respectively. The size of the specimen was decided based on the work of [19] where similar dimension (2×2×3 mm^3) was used. The sample size was also verified against the capability of the testing machines. For instance, the 3×3 mm^2 cross-section area is the calculated value for a sample that can be loaded to failure by the testing machine available in the laboratory. Also the sample is estimated to contain hundreds of grains (as grain size varied between 4 and 10 microns) and thus sufficiently large to represent the mechanical behaviour of the material at large scale (i.e., macro-scale). All samples were mounted onto a flat tungsten carbide block using hot wax and lapped on a bench-mounted KEMET 15 flat-bed diamond lapping machine (Kemet International, Maidstone, UK). The lapping was carried out on a metal plate using diamond suspensions of 45 μm, 25 μm, 8 μm and 3 μm (in a sequential order). Before the change of diamond suspension, the metal plates were fully washed/cleaned to minimize the contamination, i.e., the larger particles produced from the previous step. Then, polishing was carried out using designated soft cloths with 3 μm and then 1 μm diamond suspensions. Each lapping/polishing step took about 1 hour. Finally, the sample was hand polished using colloid silica for 20 mins. For all specimens, the ASTM-C1424-15 standard [20] was followed to ensure parallelism which is crucial for both quasi-static and dynamic compression tests.

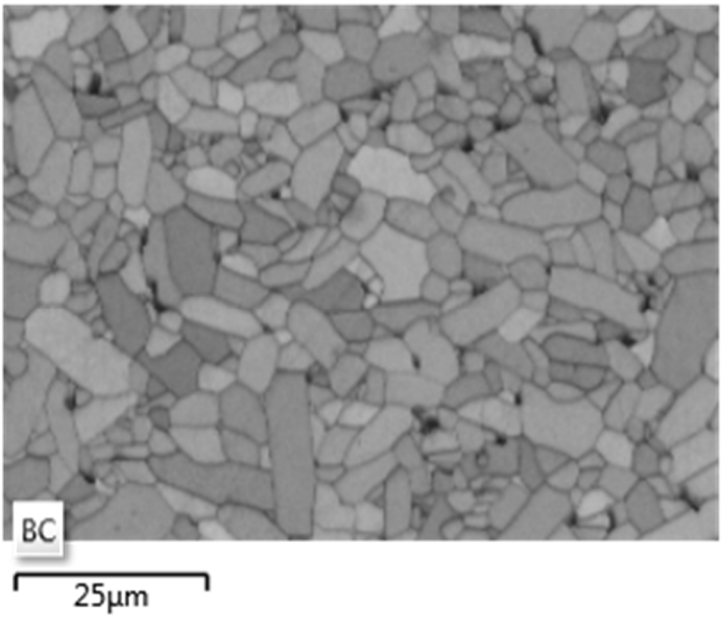

Fig. 1, Microstructure of 6H-SiC as received.

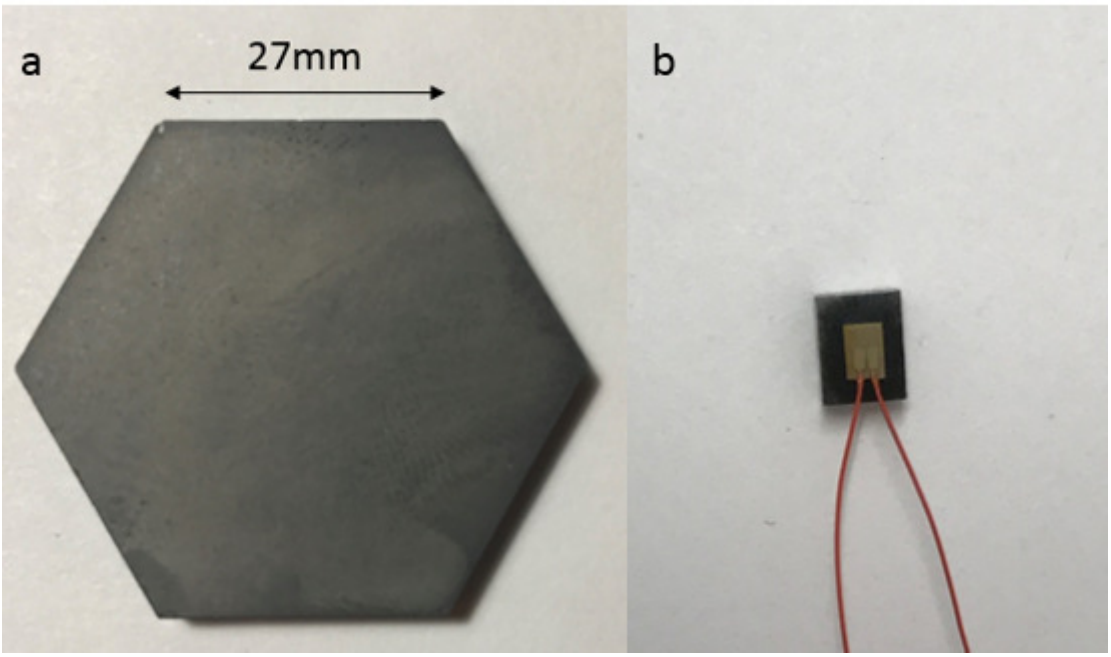

Fig. 2, (a) As-received SiC tile and (b) prepared specimen with a strain gauge mounted.

2.2 Quasi-static compression tests

The quasi-static uniaxial compression tests were carried out using an Instron 3369 universal testing machine. Tungsten carbide plates were used to protect the compression platens of the

testing machine which were made of hardened steel. A special housing was designed and carefully machined to hold the tungsten carbide (WC) plate and minimize any potential misalignment. The schematic of the setup can be seen in Fig. 3. The housing with the WC plate was connected to the load cell of the machine. Another WC plate was placed on top of the lower compression platen. Due to brittle nature of SiC, specimens fail catastrophically into small fragments in a very short time. In order to collect fragments and avoid direct contact of the two tungsten carbide plates, metal inserts with slightly shorter length than the specimen was made and placed next to the specimen. The stress was calculated according to the load applied and the cross-sectional area of the specimen. Due to compliance issues, the displacement reading from the cross-head movement was inaccurate, and therefore strain gauges were used for strain measurement in this study. The strain gauge was firmly mounted to the specimen (Fig. 2b) and connected to a meter for reading purpose.

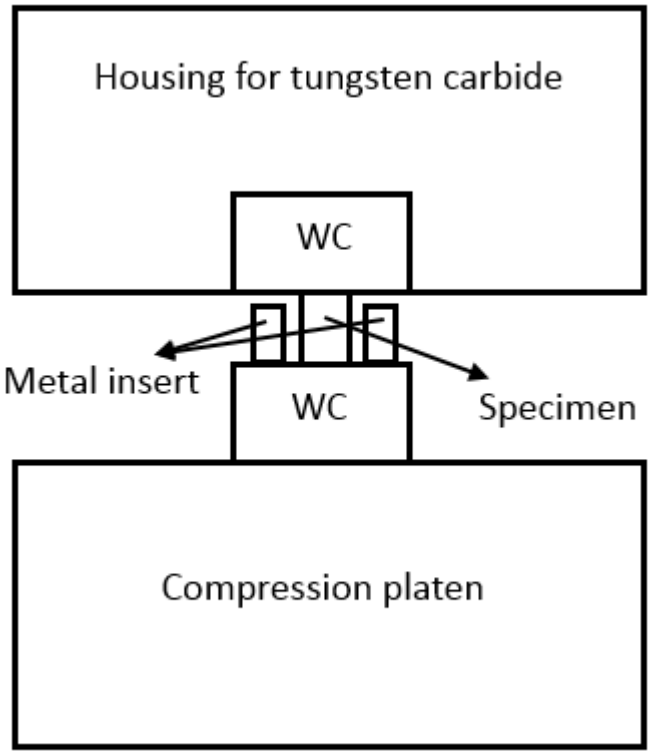

Fig. 3, Schematic of the compression test setup.

2.3 Dynamic compression tests

SHPB compression tests are widely used to study the mechanical behaviour under dynamic loading. The SHPB system involves a striker bar, an incident bar and a transmitter bar, as shown in Fig. 4. The striker bar is propelled at a high speed by a gas gun or a vacuum system to collide with the incident bar, creating an incident strain pulse. The strain pulse propagates along the incident bar until it reaches the specimen. Due to the mismatch of acoustic impedance between the bar and specimen, a portion of the pulse is reflected to the incident bar while the rest of the pulse is transmitted to the transmitter bar. These signals are captured by two strain gauges mounted on the incident and transmitted bars. Stress and strain are calculated from those signals as described below [21, 22].

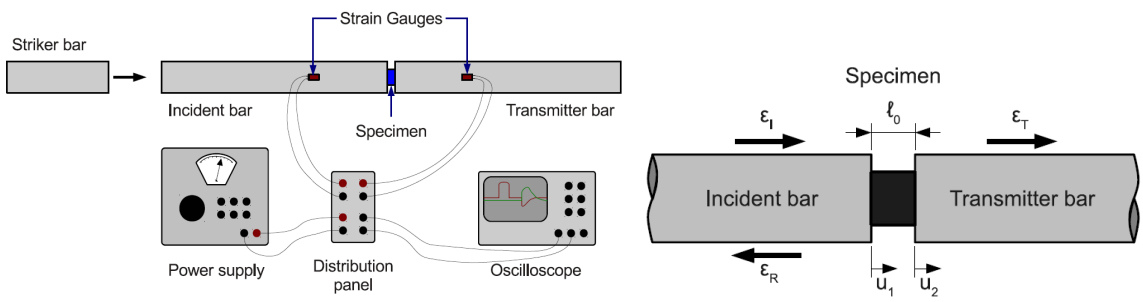

Fig. 4, A schematic of SHPB system.

As the striker bar impacts the incident bar, the force causes the incident bar to move by a distance u_1, a portion of this force leads to a deformation of the specimen and the rest leads to a movement of transmitter bar u_2 as shown in Fig. 4. The SHPB experiment is assumed to be one dimensional test, therefore the displacement u of an arbitrary point in the bar at time t is defined using one dimensional theory of elastic wave propagation:

$$u = c_0 \int_0^t \varepsilon dt \tag{1}$$

Therefore, the displacement of incident bar u_1 can be calculated using:

$$u_1 = c_0 \int_0^t \varepsilon_I dt + (-c_0) \int_0^t \varepsilon_R dt = c_0 \int_0^t (\varepsilon_I - \varepsilon_R) dt \tag{2}$$

and the displacement of the transmitter bar u_2 can be calculated using:

$$u_2 = c_0 \int_0^t \varepsilon_T dt \tag{3}$$

In the above equations, c_0 is the elastic wave velocity and $\varepsilon_I, \varepsilon_R$ and ε_T are incident strain, reflected strain and transmitted strain pulses, respectively.

The engineering strain in the specimen can be calculated as:

$$\varepsilon_{eng} = \frac{u_1 - u_2}{l_0} = \frac{c_0}{l_0} \int_0^t (\varepsilon_I - \varepsilon_R - \varepsilon_T) dt \tag{4}$$

where l_0 is the initial length of the specimen.

For simplification, it is assumed the stress across the specimen is constant, therefore:

$$\varepsilon_R = \varepsilon_T - \varepsilon_I \tag{5}$$

Thus Eq. (4) becomes

$$\varepsilon_{eng} = \frac{-2c_0}{l_0} \int_0^t \varepsilon_R dt \tag{6}$$

And the strain rate can be calculated as

$$\frac{d\varepsilon_{eng}}{dt} = \frac{-2c_0}{l_0} \varepsilon_R \tag{7}$$

The forces on both faces of the specimen are

$$F_1 = EA(\varepsilon_I + \varepsilon_R) \quad and \quad F_2 = EA\varepsilon_T \tag{8}$$

where E is the elastic modulus and A is the cross-sectional area of the pressure bars. Both E and A were assumed to be the same for the bars. Hence, the average stress in the specimen can be calculated as:

$$\sigma_{average} = \frac{F_1+F_2}{2A_s} = \frac{1}{2}E\frac{A}{A_s}(\varepsilon_I + \varepsilon_R + \varepsilon_T) \quad (9)$$

where A_s is the cross sectional area of the specimen.

Combining Eq. (5) and Eq. (9) gives

$$\sigma_{average} = \frac{EA}{A_s}\varepsilon_T \quad (10)$$

Therefore, the engineering stress is proportional to the directly transmitted strain pulse ε_T, and the engineering strain is directly proportional to the reflected strain pulse ε_R. In this paper, instead of a vacuum system, a compressed gas system was used to propel the striker bar. In order to obtain a stress equilibrium, pulse shaper made of aluminium was used for the tests. Wave signals were captured using strain gauges mounted to the incident bar and transmitted bar for later calculation of stress and strain. Different strain rates (in the order of 10^2 and 10^3 /s) were used. Fragments from those tests were collected for post-test analysis including SEM and TEM to study the dynamic behaviour of silicon carbide.

2.4 FIB lift-out for TEM analyses

In order to examine plastic deformation after testing, FIB (focused ion beam) lift-out was carried out for TEM studies. A randomly chosen fragment was placed on a sample holder with silver paste as the adhesive and solidified for 24 hours. Next, the sample was put on the stage of FIB machine, and an area of interest was chosen under electron beam mode with a voltage, current and aperture size of 10 kV, 2.1 nA and 30 μm, respectively. Once the area was selected, a layer of platinum was deposited for protection. Two trenches were created by ion beam sputter, with a 2-

3 μm gap to avoid FIB damage to the lamella as these trenches were milled under 30 kV voltage and 20 nA current. After the trenches were milled, smaller energy beam was used to clean or remove FIB damaged area resulting in a smoother finishing. The sample was then tilted, and the bottom and left-hand side of the lamella were cut loose under 30 kV voltage and 3 nA current. Following the insertion of a lift-out needle, the lamella was attached to the needle using 30 kV voltage and 30 pA current. Once the lamella was fixed to the needle by platinum, the rest region connected to the substrate was FIB milled and the lamella was removed from the base material. The removed lamella was then stuck onto a grid for final thinning. To minimize the FIB damage to the lamella, the current used was very low compared to that used for large area milling. Specifically, a current of 1 nA was used until the lamella thickness reached 1 μm, and then reduced to 0.5 nA and 0.3 nA for a thickness of 600 nm and 200 nm, respectively. Finally, a current of 100 pA was used to achieve a thickness below 200 nm. In this study, the achieved thickness was between 150 nm and 180 nm, which was sufficient for TEM scan.

3. Finite element analysis

3.1 Description of JH2 model

Although experimental testing is always necessary for determining the mechanical behaviour of materials, there are considerable motivations for the development of numerical models. With regard to the impact on ceramics, the response of the ceramic is dependent on many parameters such as projectile velocity, mechanical properties of the ceramic and substrate material that supports the ceramic sample [23]. Johnson-Holmquist model 1 (JH1) was developed for brittle materials in 1992 [24], which considered strain rate effect including the pressure-dependent strength, damage and fracture. However, this model did not consider gradual softening and as a result, the JH2 model was developed [25].

In JH2 model, the normalized equivalent stress σ^* is given as:

$$\sigma^* = \sigma_i^* - D(\sigma_i^* - \sigma_f^*) \tag{11}$$

where D is a scalar damage parameter, σ_i^* is the normalized intact equivalent stress and σ_f^* is the normalised fracture stress.

The normalized equivalent stresses have the general form:

$$\sigma^* = \sigma/\sigma_{HEL} \tag{12}$$

where σ is the actual equivalent stress and σ_{HEL} is the equivalent stress at the Hugoniot Elastic Limit (HEL).

The normalized intact and fracture strengths are given by:

$$\sigma_i^* = A(P^* + T^*)^N(1 + Cln\dot{\varepsilon}^*) \leq \sigma_i^{max} \tag{13}$$

$$\sigma_f^* = B(P^*)^M(1 + Cln\dot{\varepsilon}^*) \leq \sigma_f^{max} \tag{14}$$

where A, B, C, M and N are dimensionless material parameters, σ_i^{max} is the maximum normalized intact equivalent strength and σ_f^{max} is the maximum normalised fracture strength.

The normalised strain rate ($\dot{\varepsilon}^*$), pressure (P^*) and maximum tensile hydrostatic pressure (T^*) are defined as:

$$\dot{\varepsilon}^* = \dot{\varepsilon}/\dot{\varepsilon}_0, P^* = P/P_{HEL}, T^* = T/P_{HEL} \tag{15}$$

where, $\dot{\varepsilon}$ and $\dot{\varepsilon}_0$ are actual and reference strain rates, respectively, P is the actual pressure, T is the maximum tensile pressure that the material can withstand and P_{HEL} is the pressure at HEL.

Damage in JH2 model is assumed to accumulate through incremental plastic strain $\Delta\varepsilon^P$ of the ceramic given by:

$$D = \sum \Delta\varepsilon^P/\varepsilon_f^P \tag{16}$$

where ε_f^P is the equivalent plastic strain to fracture under a constant pressure. It can be expressed as:

$$\varepsilon_f^P = D_1(P^* + T^*)^{D_2},\ \varepsilon_{f,min}^P \leq \varepsilon_f^P \leq \varepsilon_{f,max}^P \tag{17}$$

where D_1 and D_2 are two dimensionless constants, and $\varepsilon_{f,min}^P$ and $\varepsilon_{f,max}^P$ denote the minimum and maximum equivalent plastic strains at fracture, respectively.

Before fracture happens (D =0), the hydrostatic pressure is expressed as:

$$P = K_1\mu + K_2\mu^2 + K_3\mu^3 \qquad if\ \mu \geq 0$$

$$P = K_1\mu \qquad if \mu \leq 0 \tag{18}$$

where K_1 is the bulk modulus (GPa), K_2 and K_3 are constants (GPa), and μ is the volumetric strain defined in terms of initial (ρ_0) and final (ρ) densities as:

$$\mu = \frac{\rho}{\rho_0} - 1 \tag{19}$$

When damage begins to accumulate ($D > 0$), bulking should be taken into account, and therefore, an additional incremental pressure ΔP is added:

$$P = K_1\mu + K_2\mu^2 + K_3\mu^3 + \Delta P \tag{20}$$

The pressure increment from a time t to $t + \Delta t$ is determined by:

$$\Delta P_{t+\Delta t} = -K_1\mu_{t+\Delta t} + \sqrt{(K_1\mu_{t+\Delta t} + \Delta P_t)^2 + 2\beta K_1 \Delta U} \tag{21}$$

where β is the fraction of the elastic energy loss (ΔU) converted to potential hydrostatic energy ($0 \leq \beta \leq 1$).

The elastic energy U is expressed as:

$$U = \sigma^2/6G \tag{22}$$

where σ is the equivalent plastic flow stress and G is the shear modulus. More specific details of JH2 model can be found in [25]. The basic flow chart of the JH2 model is summarized in Fig. 5.

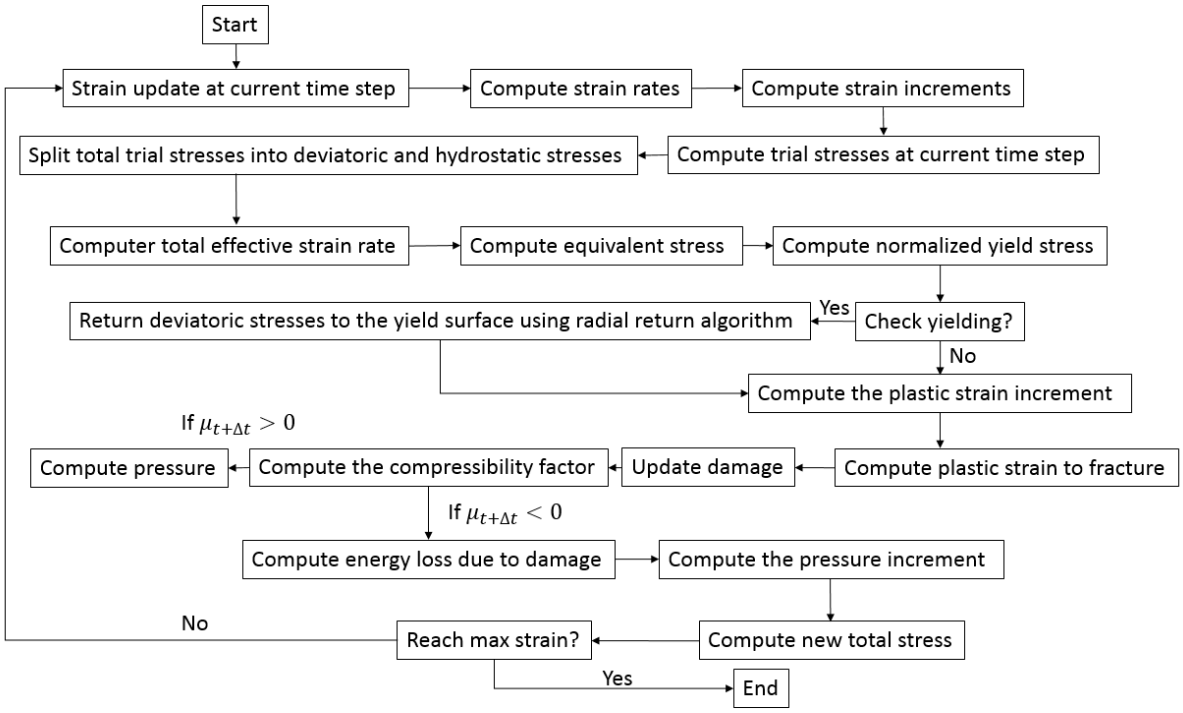

Fig. 5, Flow chart of the JH2 model.

3.2 Model setup

Abaqus/Explicit 6.14 was used as a platform for the JH2 modelling. The size of the model in the simulation is the same as that used in SHPB experiments (6×6×4 mm^3). The material was assumed to be homogeneous. Due to the larger cross-sectional area of the bars compared to the specimen (SHPB), a uniform loading was assumed to act on the specimen surface in JH2 modelling. No contact between the bars and specimen was considered here, and therefore the friction was neglected. In the initial step, the bottom surface was fixed in all directions and in loading step, a uniform velocity field was applied to the top face along the negative Y direction (compression). The boundary conditions were modified in the loading step. Specifically, the bottom face was only fixed in the Y direction, so that the material was allowed to expand in both

X and Z directions. In addition, the centre of the bottom face is fixed in X and Z directions. The element size was chosen to be 0.2 mm in this study based on a balance of the computational cost and the simulation accuracy.

4. Results and discussion

4.1 Stress-strain response

The stress-strain behaviour is compared in Fig. 6 for both the quasi-static and dynamic compression tests. The Young's modulus calculated from the stress-strain curves ranged from 393 GPa to 425 GPa which matches the value in literature [9, 12, 26-28]. For the quasi-static compression, the curves are quite linear indicating there is no evident plastic deformation. When the load exceeded the compression strength of SiC (ranges between 3.6 GPa to 4.3 GPa), it failed catastrophically into small fragments. For dynamic compression with a strain rate of 500/s, the failure stress was around 5 GPa, which was slightly larger than that for quasi-static compression. The failure stress increased up to 6 GPa when the strain rate increased to 2000/s, which implies strong strain-rate sensitivity of the material. A similar phenomenon had been reported elsewhere [9, 19, 28]. The 'plateau' regions of the stress-strain curves represent the reflected signals in the SHPB system after the sample was crushed, and may be caused by accumulation of plastic deformation and damage.

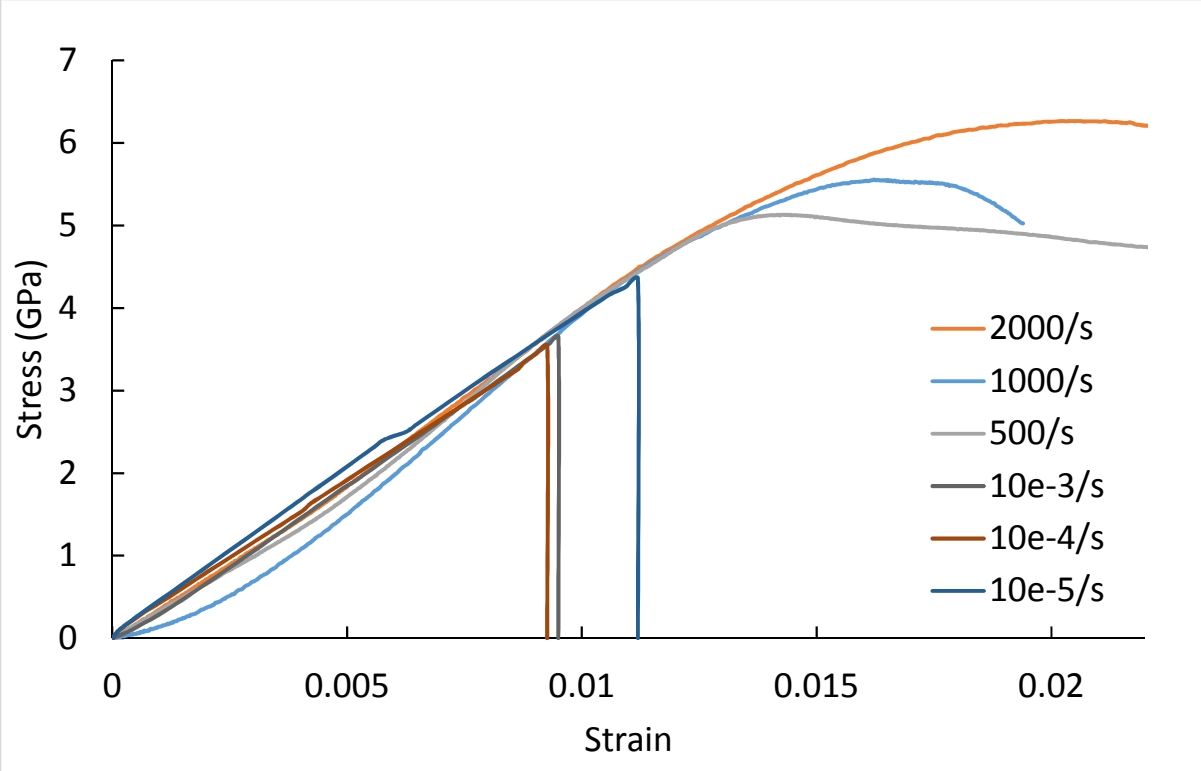

Fig. 6, Stress-strain curves from quasi-static and SHPB compression experiments.

4.2 SEM and TEM analysis

The fracture of grains (transgranular fracture) and the failure of grain boundaries (intergranular fracture) are two possible fracture modes in ceramics depending on the material itself and the loading condition [9, 28]. To better understand the SiC failure mode under different loading conditions, Field Emission Gun Scanning Electron Microscopy (FEGSEM) was used to study the fracture mechanisms. Fragments were collected after both quasi-static and dynamic compression tests for SEM examination. The fragment size is largely different for the two testing regimes. Large pieces (1-2 mm) of fragments were produced from static compression whereas the fragments were much smaller (in microns) in SHPB tests. This implies that micro-cracking was dominant during compression under higher strain rate. Figures 7 (a-b) and (c-d) show the SEM images of fragments collected from quasi-static and dynamic compression tests, respectively. As can be seen, for quasi-static compression tests, the cracked surfaces shown in

Fig. 7(a-b)) were quite smooth (no debris) and the fragment size is much larger than the grain size (4-10 μm) of the specimen. This implies intergranular fracture of the sample, and that failure tends to occur along the grain boundaries due to weak interfacial strength. For dynamic loading, the fragments were much smaller (less than a grain) and also covered with even smaller pieces of debris, as shown in Fig. 7(c-d). This implies that the energy built up during a dynamic compression test is sufficient to split grains and cause transgranular fracture [29, 30].

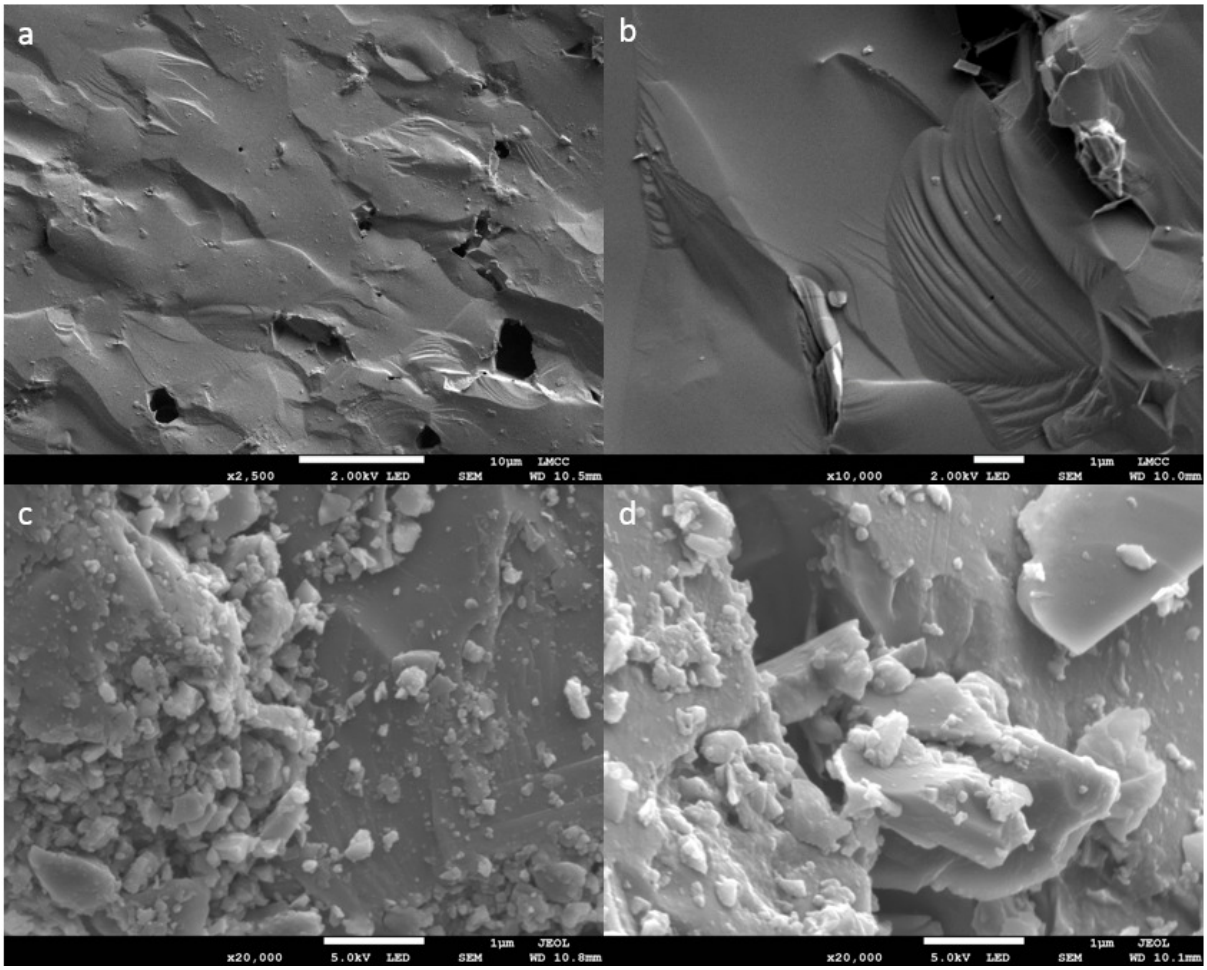

Fig. 7, SEM images of fragments collected from (a-b) quasi-static and (c-d) dynamic compression tests.

In order to confirm if plastic deformation takes place under such loading condition, FIB lift-outs were carried out for fragments collected after quasi-static and dynamic uniaxial compression tests. Figure 8 gives selective TEM images from a randomly chosen fragment after quasi-static compression test. Figure 8(a) shows the overall lamella lifted out. This image shows a clear view of the sample microstructure such as the grain size, voids and grain boundaries. In particular, Fig. 8(b) shows the boundaries between grains and inclusions or cavities where dislocations tend to nucleate. Despite through studies, there was no evidence of dislocations or plastic-deformation related defects.

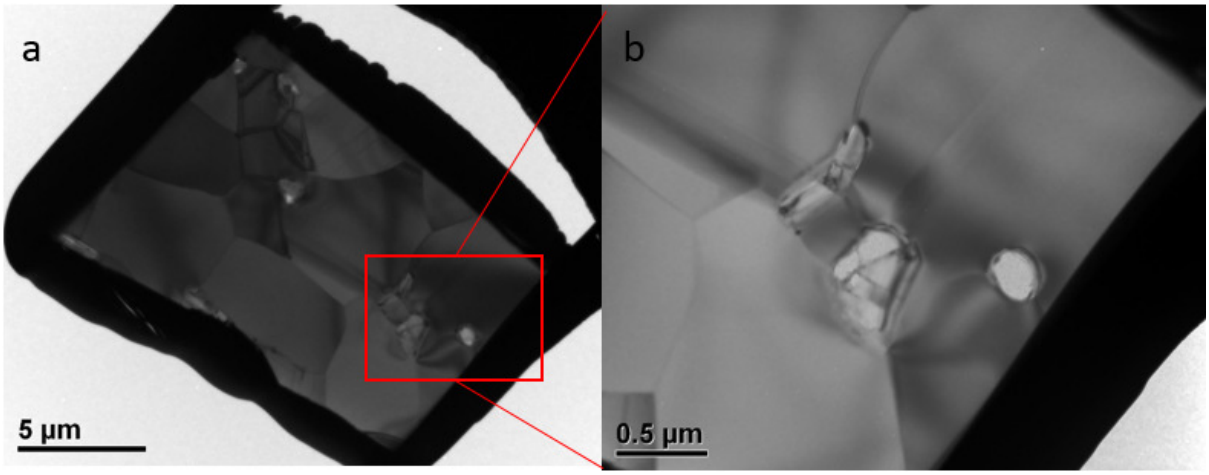

Fig. 8, TEM images of lift-out lamella from fragments collected after quasi-static compression test.

Similar FIB lift-out and TEM analysis were performed for fragments collected from the SHPB experiments under different loading rates. Figures 9(a-b), (c-d) and (e-f) present selective TEM images for samples tested under a strain rate of 500/s, 1000/s and 2000/s, respectively. Examinations were carried out across all the lift-out lamella with a focus on finding plastic deformation related defects such as dislocations and kinks. For 500/s strain rate, voids were presented in the lamella produced by FIB (see Figure 9(a)). The large void could be caused

during the FIB operation, especially when high residual stresses were present in the region; whereas the small voids were formed during the sintering process. "Shear bands" were noticed at the boundaries between grains and voids (yellow circle in Figure 9(b)), which had different orientations due to different grain orientations. These "shear bands" were in fact stacking faults, similar to the observations reported in [28] and [31]. Stacking fault energy in 6H-SiC was estimated to be 1.9-2.5 mJ/m^2 which is two orders less than that for metals [32-34]. As a result, stacking fault can be generated more easily in 6H-SiC. For samples tested under a strain rate of 1000/s, a lot of 'black lines' can be observed in the lift-out lamella as shown in Figure 9(c). Further examinations suggested that these lines were not dislocations. However, dislocations were actually observed at grain boundaries as shown in Figure 9(d) (yellow circle). They had different orientations in the two grains (partly overlapped), and pile-ups occurred near the grain boundary. For samples tested under a strain rate of 2000/s, dislocation loops and kinks were clearly visible, especially at the grain boundaries (Figure 9(e-f), yellow circle).

According to TEM analyses, it was suggested that plastic-deformation related defects are more likely to be found in materials under high strain rate compression. For instance, no obvious dislocations were found for a specimen under quasi-static compression; whereas defects such as dislocations, kinks and shear bands can be clearly observed for samples tested under a strain rate up to 2000/s. Although dislocations were also found for the sample tested under a strain rate of 1000/s, the area being examined was larger than that for the sample tested under a strain rate of 2000/s, meaning a lower dislocation density for decreased strain rate. Plastic deformation in crystalline material is mainly caused by the generation, multiplication and movement of dislocations. When the resolved shear stresses exceeded the critical resolved shear stress, the dislocations form and glide on slip planes. For static compression tests, there was no plastic deformation and material failed by coalescence of microcracks which were nucleated at grain boundaries, voids and inclusions. Lateral confinement, either from external pressure [18] or

induced dynamically [16], can suppress the propagation of microcracks and promote localized inelastic deformation around the crack tip. For dynamic compression, the inertially induced lateral confinement is the reason for plastic deformation which is related to the localized dislocation activities as verified from our TEM studies. It is worth pointing out that all lamella were lift out from a randomly picked-up fragment due to the nature of catastrophic failure.

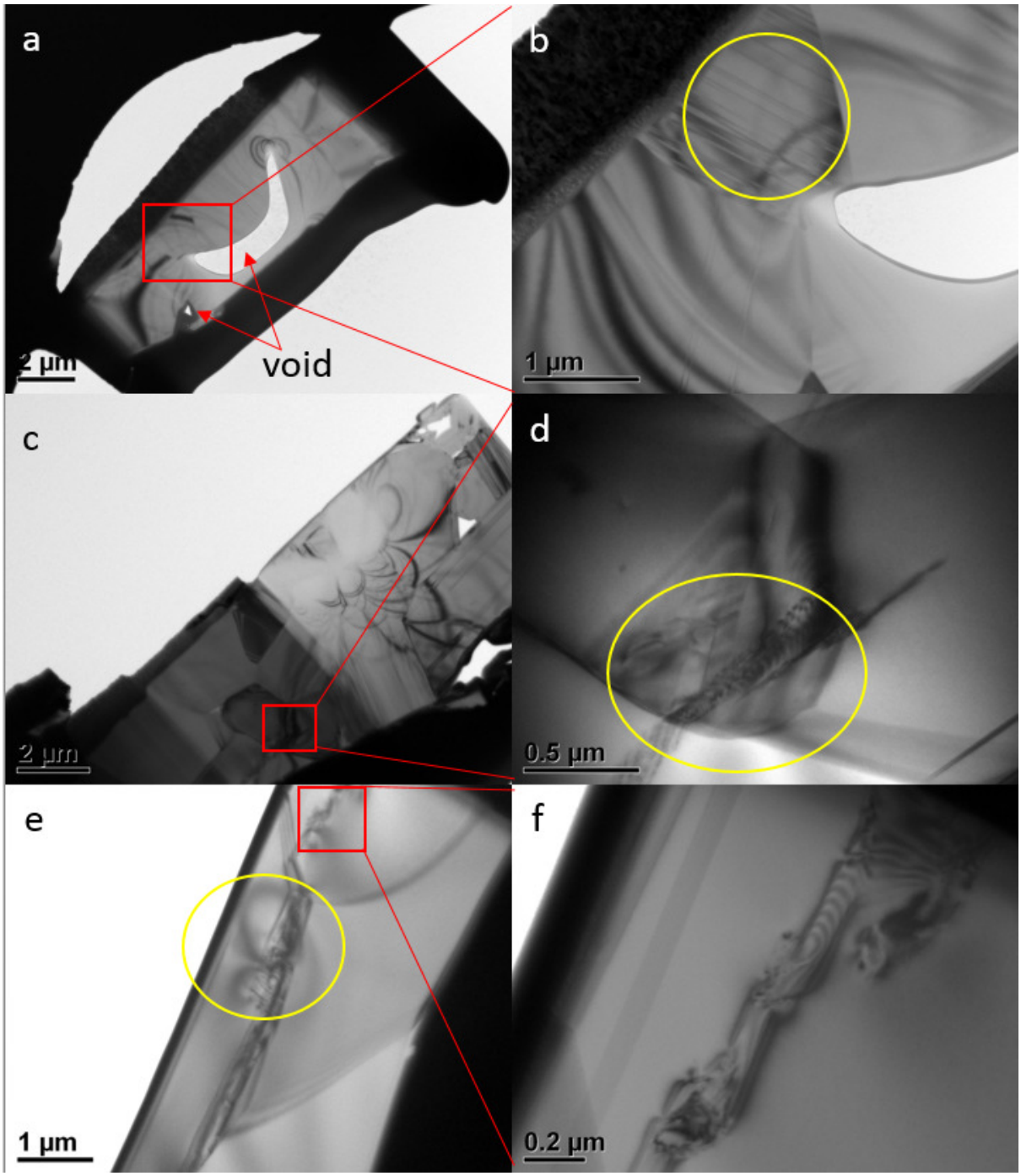

Fig. 9 TEM images of lift-out lamella from fragments collected after SHPB tests: (a-b) 500/s, (c-d) 1000/s and (e-f) 2000/s strain rate.

4.3 JH2 simulation

Model parameters were calibrated in order to match the experimental results in terms of stress-strain behaviour. To determine the model parameters, we adopt a fitting procedure based on iterative simulations of SHPB stress-strain responses for three varied loading rates (500/s, 1000/s and 2000/s). Prior to the fitting process, some fundamental material parameters such as modulus was directly obtained from experimental measurements (linear part of the stress-strain curve) and Poisson's ratio was assumed as 0.2 [11]. Initial values of other JH2 related parameters were estimated based on the literature [23, 35]. Following each simulation, the stress-strain responses were obtained and compared with those measured experimentally to assess the difference. This essentially is an inverse parameter-fitting process. Basically, we manually change the values of the parameters until the simulated stress-strain responses matched the SHPB test data for three loading rates. The procedure consisted of a series of iterations until an acceptable agreement was achieved between model simulations and experimental data. The parameters calibrated for SiC in this study are summarized in Table 1, with description given in Section 3.1. The values were in the range reported in literature [23, 24, 35]. In Table 1, i_{damage} is the initial damage of the material and FS is the failure strain required as inputs for simulations in Abaqus. The stress-strain curves from JH2 model and SHPB tests are compared in Fig. 10, showing a good match between them. The calibrated JH2 model was then used to predict the rate-dependent strength for the material and plotted in Fig. 11, in comparison with SHPB tests and also data from Lankford [9]. The JH2 predictions match the SHPB results very well, showing a strong dependency of compressive strength on strain rate. The results follow the trend reported by Lankford [9]. Figures 12 (a) and (b) show the damage contour plot at the moment of failure

for 4000/s and 500/s strain rate, respectively. It can be seen that for 4000/s loading rate, the damage is less than that for 500/s loading rate. This can be explained by the theory that there is not sufficient time for crack to nucleate in a high strain rate experiment [9, 14]. In addition, the damage for 4000/s loading rate tends to spread across the whole sample, leading to numerous smaller fragments. Whereas the damage for 500/s loading rate is very concentrated, leading to fewer but larger fragments. This is consistent with the experimental observations mentioned above. Figures 12 (c) and (d) show the contour plots of equivalent plastic strain for 4000/s and 500/s loading rates, respectively. It can be seen that the level of plastic strain is similar for both cases, but more evenly distributed for a higher loading rate (4000/s), consistent with damage evolution. It should be mentioned that different scale bar was used in the contour plots for the two cases, as the damage and plastic strain were largely different between them. If the same scale bar was adopted, one contour plot will be dominated by a single colour, losing the contrast immediately. The presented scale bar was the most suitable for better viewing of the damage and plastic strain distribution over the fragments.

Table 1, Parameters calibrated for JH2 model.

ρ_0 ($\frac{kg}{m^3}$)	G (GPa)	A	N	B	M	C	$\dot{\varepsilon}_0$ (1/s)
3125	170	0.96	0.65	0.35	1	0.09	1
T (GPa)	σ_i^{max}	σ_f^{max}	HEL(GPa)	P_{HEL}(GPa)	β		
0.75	1.24	0.132	11.7	7	1		
D_1	D_2	$\bar{\varepsilon}_{f,max}^{pl}$	$\bar{\varepsilon}_{f,min}^{pl}$	FS	IDamage		
0.48	0.48	1.2	0	0.2	0		
K_1 (GPa)	K_2(GPa)	K_3(GPa)					
220	361	0					

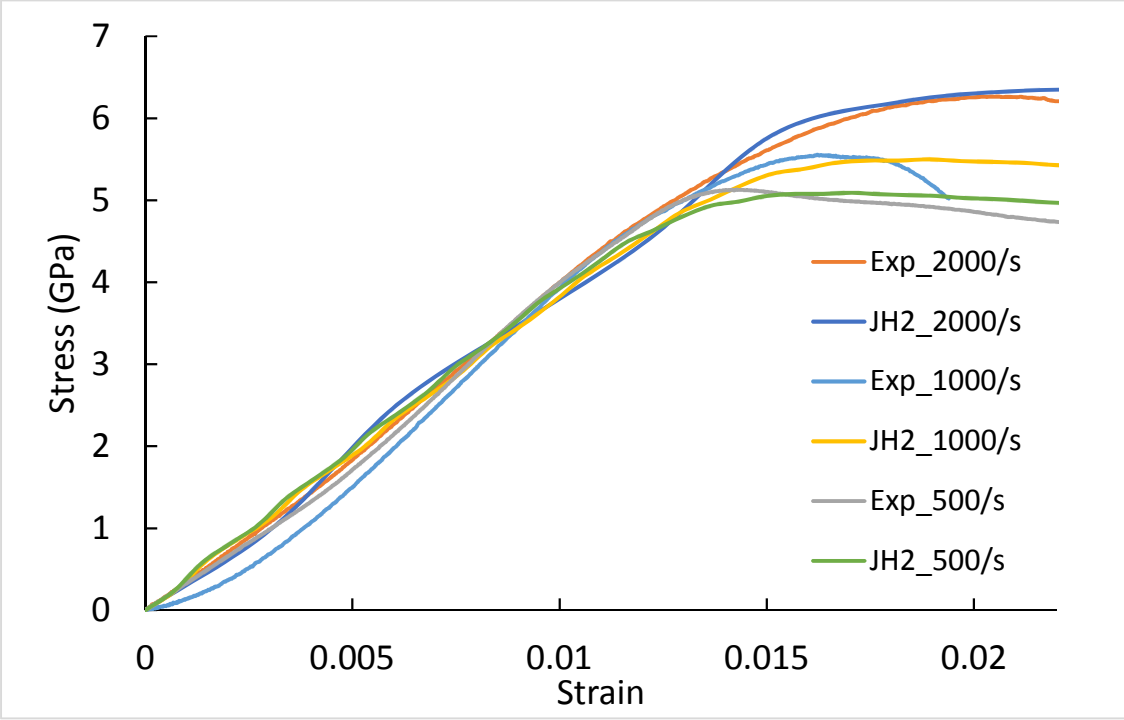

Fig. 10, Comparison of stress-strain curves obtained from JH2 model and SHPB tests.

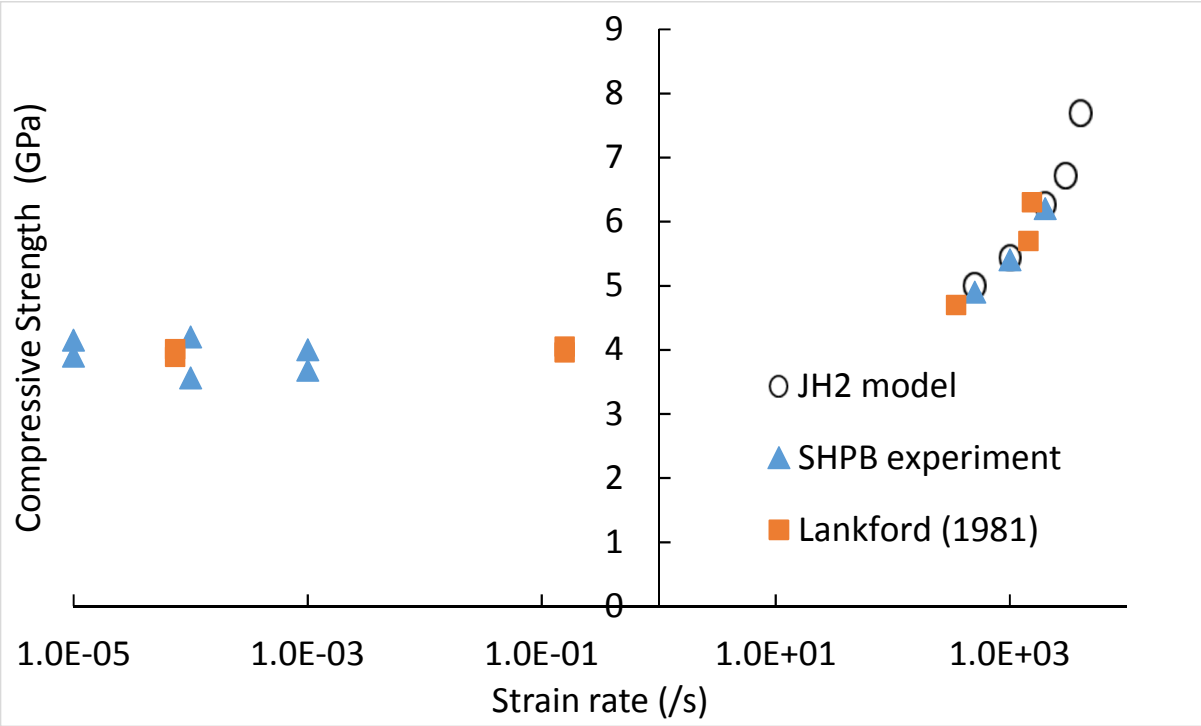

Fig. 11, Compressive strength of 6H-SiC against loading rate.

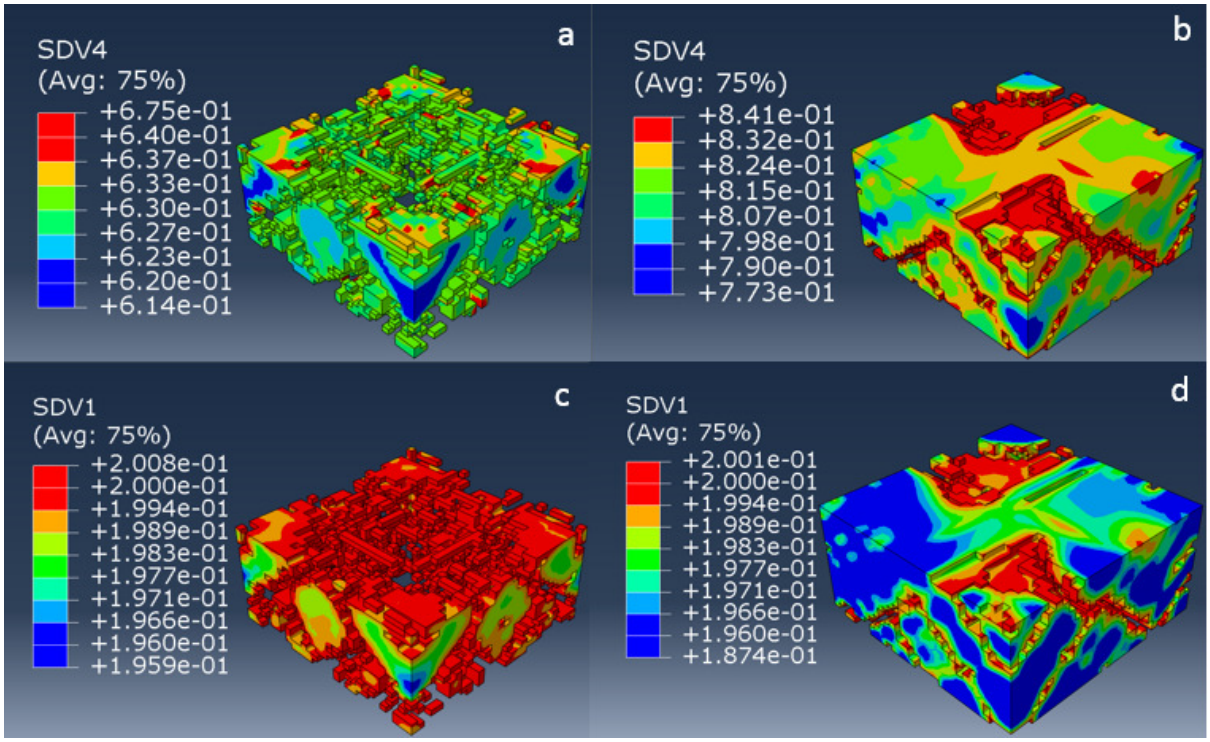

Fig. 12, Contour plots of (a-b) damage (SDV4) and (c-d) equivalent plastic strain (SDV1) at the moment of failure for 4000/s (left) and 500/s (right) loading rates, respectively.

5. Conclusion

In conclusion, uniaxial compression tests were conducted for 6H-SiC in both quasi-static and dynamic regimes. It was found that the strength of SiC is dependent on the loading rate, which increase with increasing strain rate. In addition, it was noted that higher loading rates lead to smaller fragments upon failure. This is associated with two possible fracture modes, i.e., transgranular fracture under dynamic loading and intergranular fracture under static or low-speed loading. From the TEM scans, defects such as dislocation loops, kinks and shear bands can be clearly seen in samples tested at high strain rate. For lower strain rate compression, those defects

were not obvious. In addition, the JH2 simulation was performed, with parameters calibrated against experimental results. The model was able to predict the varied dynamic strength of SiC, further supporting the rate sensitivity of SiC.

6. Acknowledgements

We are grateful for the support of Northwestern Polytechnical University (Xi'an, Shaanxi, China) for the support for SHPB tests, including access to the testing facilities and also helpful discussions.

7. References

[1] Reddy, J.D., Volinsky, A.a., Frewin, C.L., Locke, C., and Saddow, S.E., 2007, 'Mechanical Properties of 3C-SiC Films for MEMS Applications,' *MRS Proc.*, vol. 1049.

[2] Sarro, P.M., 2000, 'Silicon carbide as a new MEMS technology,' *Sensors Actuators, A Phys.*, vol. 82, no. 1, pp. 210–218.

[3] Frischmuth, T., Schneider, M., Maurer, D., Grille, T., and Schmid, U., 2016, 'Inductively-coupled plasma-enhanced chemical vapour deposition of hydrogenated amorphous silicon carbide thin films for MEMS ,' *Sensors Actuators A. Phys.*, vol. 247, pp. 647–655.

[4] Tamura, T., Nakamura, T. Takahashi, K., Araki, T. and Natsumura, T., 2005, 'Research of CMC Application to Turbine Components', *IHI Engineering Review*, vol. 38, pp. 58-62.

[5] Bian, G. and Wu, H., 2015, 'Friction and surface fracture of a silicon carbide ceramic brake disc tested against a steel pad,' *Journal of the European Ceramic Society*, vol. 35, pp. 3797–3807.

[6] Venkatesan, J., Iqbal, M.A. and Madhu, V., 2017, 'Ballistic Performance of Bilayer Alumina Aluminium and Silicon Carbide Aluminium Armours*,' Procedia Engineering*, vol. 173, pp. 671–678.

[7] Crouch, I.G., Kesharaju, M. and Nagarajah, R., 2015, 'Characterisation , significance and

detection of manufacturing defects in Reaction Sintered Silicon Carbide armour materials,' *Ceram. Int.*, vol. 41, no. 9, pp. 11581–11591.

[8] Tomono, K., Furuya, H., Miyamoto, S., Okamura, Y., Sumimoto, M., Sakata, Y., Komatsu, R. and Nakayama, M., 2013, 'Investigations on hydrobromination of silicon in the presence of silicon carbide abrasives as a purification route of kerf loss waste,' *Sep. Purif. Technol.*, vol. 103, pp. 109–113.

[9] Lankford, J., 1981, 'Mechanisms Responsible for Strain-Rate-Dependent Compressive Strength in Ceramic Materials,' *Communications of the American Ceramics Society*, pp. 5–6.

[10] Nemat-Nasser, S., and Deng, H., 1994, 'Strain-rate effect on brittle failure in compression,'*Acta metall. Mater.* vol. 42, no. 3, pp. 1013–1024.

[11] Sarva, S. and Nemat-nasser, S., 2001, 'Dynamic compressive strength of silicon carbide under uniaxial compression,' *Materials Science and Engineering*, vol. 317, pp. 140–144.

[12] Garkushin, G.V., Razorenov, S.V., Rumyantsev, V.I. and Savinykh, A.S., 2014, 'Dynamic Strength of Reaction-Sintered Silicon Carbide Ceramics,' *Mechanics of Solids*, vol. 49, no. 6, pp. 616–622.

[13] Holland, C. and Mcmeeking, R.M., 2015, 'The influence of mechanical and microstructural properties on the rate-dependent fracture strength of ceramics in uniaxial compression,' *Int. J. Impact Eng.*, vol. 81, pp. 34–49.

[14] Pittari, J., Subhash, G., Zheng, J., Halls, V. and Jannotti, P., 2015, 'The rate-dependent fracture toughness of silicon carbide- and boron carbide-based ceramics,' *J. Eur. Ceram. Soc.*, vol. 35, no. 16, pp. 4411–4422.

[15] Castaing, J., Cadoz, J., and Kirby, S.H., 1978, 'Prismatic Slip of Al_2O_3 Single Crystals Below 1000 ° C in Compression Under Hydrostatic Pressure,' *Journal of the American Ceramic Society*, vol. 64, no. 9, pp. 504–511.

[16] Lankford, J., 1981, 'Temperature-strain rate dependance of compressive strength and damage mechanisms in aluminium oxide,' *Journal of Materials Science*, vol. 16, pp. 1567–

1578.

[17] Louro, L.H.L., and Meyers, M.A., 1989, 'Effect of stress state and microstructural parameters on impact damage of alumina-based ceramics,' *Journal of Materials Science*, vol. 24, pp. 2516-2532.

[18] Chen, W. and Ravichandran, G., 1996, 'Static and Dynamic Compressive Behavior of Aluminum Nitride under Moderate Confinement', *Journal of the America Ceramic Society*, vol 79, issue 3, pp. 579-584.

[19] Wananuruksawong, R., Shinoda, Y., Akatsu, T. and Wakai, F., 2015, 'High-strain-rate superplasticity in nanocrystalline silicon nitride ceramics under compression,' *Scr. Mater.*, vol. 103, pp. 22–25.

[20] ASTM C1424-15, Standard Test Method for Monotonic Compressive Strength of Advanced Ceramics at Ambient Temperature, *ASTM International*, West Conshohocken, PA, 2015, www.astm.org.

[21] Kolsky, H., 1949, 'An Investigation of Mechanical Properties of Material at very High Rates of loading', *Proceeding of the Physical Society*, Section B, Vol. 62, Number 11.

[22] Frew, D.J., Forrestal, M.J., Chen, W., 2000, 'A split Hopkinson pressure bar technique to determine compressive stress-strain data for rock materials', *Experimental Mechanics*, Vol. 41, Issue 1, pp 40-46.

[23] Cronin, D.S., Bui, K., Kaufmann, C., Mcintosh, G., Berstad, T., and Cronin, D., 'Implementation and Validation of the Johnson-Holmquist Ceramic M aterial Model in LS-Dyna, 4th European LS-DYNA Users Conference, pp. 47–60.

[24] G.R. Johnson and T.J. Holmquist, 1992, 'A Computational Constitutive Model for Brittle Materials Subjected to Large Strains, High Strain Rates and High Pressures', Shock-Wave and High-Strain-Rate Phenomena in Materials, edited by M.A. Meyers, L.E. Muir, and K.P. Staudhammer, Marcel Dekker Inc., New York, pp. 1075-1081.

[25] Johnson, G.R. and Holmquist, T.J., 1994, 'An improved computational constitutive model for brittle materials,' *American Institute of Physics*, vol. 981, pp. 1–5.

[26] Hayun, S., Paris, V., Mitrani, R., Kalabukhov, S., Dariel, M.P.P., Zaretsky, E. and Frage, N., 2012, 'Microstructure and mechanical properties of silicon carbide processed by Spark Plasma Sintering (SPS),' *Ceram. Int.*, vol. 38, no. 8, pp. 6335–6340.

[27] Forquin, P. and Denoual, C., 2003, 'Experiments and modelling of the compressive behaviour of two SiC ceramics,' *Mechanics of Materials*, vol. 35, pp. 987–1002.

[28] Shin, C.J., Meyers, M.A., Nesterenko, V.F. and Chen, S.J., 2000, 'Damage evolution in dynamic deformation of Silicon carbide,' *Acta mater.* vol. 48, pp. 2399-2420.

[29] Hu, G., Chen, C.Q., Ramesh, K.T. and McCauley, J.W., 2012, 'Mechanisms of dynamic deformation and dynamic failure in aluminium nitride', *Acta material*, Vol. 60, pp. 3480-3490

[30] Wang, Z. and Li, P., 2015, 'Dynamic failure and fracture mechanism in alumina ceramics : Experimental observations and fi nite element modelling,' *Ceram. Int.*, Vol. 41, issue 10, pp. 12763–12772.

[31] Zhou, Y.C., He, L.F., Lin, Z.J. and Wang, J.Y., 2013, 'Synthesis and Structure–Property Relationships of a New Family of Layered Carbides in Zr-Al(Si)-C and Hf-Al(Si)-C Systems', *Journal of European Ceramic Society*, Vol 33, pp. 2831-2865.

[32] Stevens, R., 1972,'Defects in silicon carbide', *Journal of Materials Science*, vol. 7, issue 5, pp. 517-521.

[33] Maeda, K., Suzuki, K., Fujita, S., Ichihara, M. and Hyodo, S., 1988, 'Defects in plastically deformed 6H-SiC single crystal studied by transmission electron microscopy', *Philosophical Magazine A: Physics of Condensed Matter, Structure, Defects and Mechanical Properties*, vol 57, issue 4, pp. 573-592.

[34] Weertman, J., Weertman, J.R., 1992, 'Elementary Dislocation Theory', Oxford University Press, New York. pp. 98.

[35] Holmquist, T.J. and Johnson, G.R., 2008, 'Response of silicon carbide to high velocity impact Response of silicon carbide to high velocity impact,' *Journal of Applied Physics,* vol. 91, no. 9, pp. 5858-5866.